Available online at www.sciencedirect.com
SCIENCE DIRECT®
Planetary and Space Science 52 (2004) 733–746
Planetary and Space Science
www.elsevier.com/locate/pss

Determination of the properties of Mercury's magnetic field by the MESSENGER mission

Haje Korth[a,*], Brian J. Anderson[a], Mario H. Acuña[b], James A. Slavin[b], Nikolai A. Tsyganenko[b], Sean C. Solomon[c], Ralph L. McNutt Jr.[a]

[a] *Applied Physics Laboratory, The Johns Hopkins University, 11100 John Hopkins Road, Laurel, MD 20723-6099, USA*
[b] *NASA Goddard Space Flight Center, Greenbelt, MD 20771, USA*
[c] *Carnegie Institution of Washington, Department of Terrestrial Magnetism, 5241 Broad Ranch Road, N.W., Washington, DC 20015, USA*

Received 27 March 2003; received in revised form 20 November 2003; accepted 18 December 2003

Abstract

The MESSENGER mission to Mercury, to be launched in 2004, will provide an opportunity to characterize Mercury's internal magnetic field during an orbital phase lasting one Earth year. To test the ability to determine the planetary dipole and higher-order moments from measurements by the spacecraft's fluxgate magnetometer, we simulate the observations along the spacecraft trajectory and recover the internal field characteristics from the simulated observations. The magnetic field inside Mercury's magnetosphere is assumed to consist of an intrinsic multipole component and an external contribution due to magnetospheric current systems described by a modified Tsyganenko 96 model. Under the axis-centered-dipole approximation without correction for the external field the moment strength is overestimated by $\sim 4\%$ for a simulated dipole moment of 300 nTR_M^3, and the error depends strongly on the magnitude of the simulated moment, rising as the moment decreases. Correcting for the external field contributions can reduce the error in the dipole term to a lower limit of ~ 1–2% without a solar wind monitor. Dipole and quadrupole terms, although highly correlated, are then distinguishable at the level equivalent to an error in the position of an offset dipole of a few tens of kilometers. Knowledge of the external magnetic field is therefore the primary limiting factor in extracting reliable knowledge of the structure of Mercury's magnetic field from the MESSENGER observations.

Keywords: Mercury; MESSENGER mission; Magnetic field; Multipole inversion

1. Introduction

Characterizing the nature of planetary magnetic fields is important for broadening our understanding of planetary origins and evolution and of the energetics and life-times of magnetic dynamos. A planet of great interest regarding its magnetic properties is Mercury, whose intrinsic magnetic field was discovered during two flybys of the Mariner 10 spacecraft in 1974 and 1975. Possible sources for Mercury's magnetic field are thermoremanence, an active dynamo, or a combination thereof. Thermoremanent magnetization may have been induced either by a large external (solar or nebular) magnetic field or by an internal dynamo that existed earlier in the planet's evolution. The former process seems implausible since any early solar or nebular field would presumably have decayed on timescales much faster than the timescale for thickening of Mercury's lithosphere (Stevenson, 1987). The latter hypothesis of an early dynamo being the source for thermoremanent magnetization at Mercury seems at first unconvincing, because of the magnetostatic theorem by Runcorn (1975a,b) that prohibits the existence of a magnetic field external to the planet after dynamo activity has ceased. However, Runcorn's theorem is valid only under ideal conditions and is violated if a non-uniform permeability is assumed (Stephenson, 1976), cooling of the planetary interior occurred progressively inward rather than instantaneously (Srnka, 1976), or asymmetries persist in the thermal structure of the lithosphere (Aharonson et al., 2004). The alternative source of Mercury's magnetic field is a still active dynamo. Although thermal evolution models predict the solidification of a pure iron core early in Mercury's history (Solomon, 1976), it has been argued that even small quantities of light alloying elements, such as sulfur or oxygen, could have prevented the

* Corresponding author. Fax: +1-443-778-0386.
E-mail address: haje.korth@jhuapl.edu (H. Korth).

0032-0633/$ - see front matter © 2004 Elsevier Ltd. All rights reserved.
doi:10.1016/j.pss.2003.12.008

core from freezing out (Stevenson et al., 1983). Therefore, the hypothesis of an active hydrodynamic (Stevenson, 1983) or thermoelectric dynamo (Stevenson, 1987; Giampieri and Balogh, 2002) operating at Mercury is still viable. The above source mechanisms imply distinct characteristics for the structure of the magnetic field. In order to distinguish among them, a detailed mapping of the main field, as well as of the crustal fine structure, is required.

The Mariner 10 spacecraft obtained measurements of Mercury's magnetic field during two of three Mercury flybys on March 29, 1974 (encounter I), and March 16, 1975 (encounter III). On encounter I, the spacecraft made its closest approach to the planet at an altitude of 705 km on the nightside of the planet near the equator. The maximum magnetic field strength measured on this flyby was 98 nT (Ness et al., 1974, 1975). Encounter III was targeted closer to the planet, with a closest approach altitude of 327 km at 68°N latitude. The highest field strength detected on this flyby was 400 nT (Ness et al., 1976; Lepping et al., 1979). Encounter II, on September 21, 1974, was designed to optimize imaging observations and came only within 5×10^4 km of the planetary dayside surface. It showed no evidence of any planetary field.

Several groups have estimated the magnetic moment of Mercury from the observations made during the two close flybys. Conducting a least-squared fit of the Mercury encounter I flyby data to an offset tilted dipole, Ness et al. (1974) obtained a dipole moment of 227 nTR_M^3, where $R_M =$ 2439.7 km is the planetary radius of Mercury. Ness et al. (1975) considered a centered dipole and an external contribution to the measured magnetic field and found the strength of the dipole to be 349 nTR_M^3 for the same data set. From the Mercury encounter III observations these authors determined a dipole moment of 342 nTR_M^3 (Ness et al., 1976). Higher-order contributions to the internal magnetic field were examined by Jackson and Beard (1977) (quadrupole) and Whang (1977) (quadrupole, octupole). Both sets of authors reported 170 nTR_M^3 as the dipole contribution to Mercury's intrinsic magnetic field.

The large spread in the reported estimates of the dipole term is due to the non-unique nature of the inversion problem, caused by geometric constraints of the Mariner 10 trajectories. As a consequence, not all model parameters of the spherical harmonic expansion can be determined independently from each other. For example, there is a linear relationship between the dipole coefficient g_1^0 and the quadrupole term g_2^0 in the spherical harmonic expansion (Connerney and Ness, 1988). It is impossible to separate these terms using the Mariner 10 data, and detailed knowledge of the intrinsic field will require observations from a planetary orbiter.

The Mariner 10 observations showed that the modest internal magnetic field of Mercury is sufficient to deflect the solar wind flow around the planet (Siscoe and Christopher, 1975), and the magnetic field and electron observations indicate the existence of an Earth-like magnetosphere (Ness et al., 1974,1975; Ogilvie et al., 1975). However, its dimensions perpendicular to the planet-sun line are only 5% of those of the Earth, because the magnetic moment of Mercury is more than 1000 times smaller than the terrestrial moment, the solar wind density is higher, and the interplanetary magnetic field (IMF) is stronger at Mercury than at 1 AU (Russell et al., 1988). As a consequence, the magnetic fields from magnetospheric currents at Mercury are of the same order as the intrinsic field and vary significantly in response to the local solar wind and IMF (Luhmann et al., 1998). Careful account for the external field will therefore have to be made to determine the structure of Mercury's intrinsic magnetic field.

Extensive measurements of the magnetic field near Mercury will be provided by the MErcury Surface, Space ENvironment, GEochemistry, and Ranging (MESSENGER) mission (Solomon et al., 2001). To be launched in 2004, the MESSENGER spacecraft will orbit Mercury for one Earth year. The MESSENGER orbit has an initial periapsis altitude of 200 km and an initial latitude of periapsis of 60°N; the orbit is inclined 80° to the equatorial plane of the planet and has a 12-h period (Santo et al., 2001). In the March 2004 launch scenario, the orbital phase lasts from April 6, 2009, until April 6, 2010, after completing two flybys of that planet following two flybys of Venus. The flybys in July 2007 and April 2008 return significant new data early in the mission, while the orbital phase, beginning in April 2009, enables a focused scientific investigation of the planet, guided by the flyby data.

In order to characterize Mercury's magnetic field, MESSENGER is equipped with a three-axis, ring-core fluxgate magnetometer (MAG), mounted on a 3.6-m boom in an anti-sunward direction (Gold et al., 2001). The MAG instrument samples the magnetic field at 20 samples per second. However, the rate of data transmitted will depend on the telemetry link margin. Emphasis during data collection will be on the periapsis passes, where the planetary contribution to the ambient field is greatest. As the planet rotates beneath the orbit of the spacecraft, 360°-mapping of the magnetic field is achieved in the northern hemisphere with a longitudinal track spacing of $\sim 3°$ between consecutive orbits. This enhanced coverage of magnetic field observations should reduce the present ambiguity in the multipole parameters described by Connerney and Ness (1988). The extended period of observations, including observations in both the magnetosphere and solar wind, will provide a wealth of data on the magnetospheric current systems at Mercury.

In this paper we assess how accurately the MESSENGER observations will constrain Mercury's magnetic moment including the effects of the external magnetic field. This is a natural extension of the inversion calculations of Giampieri and Balogh (2001), who examined multipole inversions from a simulated BepiColombo mission to Mercury. Their focus was on recovering different internal magnetization structures in the absence of an external field. We are specifically treating the effects of the external field, including estimates for the intensity and variability that are as re-

alistic as possible at present. This approach allows us to estimate the errors introduced by the external field, which Giampieri and Balogh (2001) did not consider. We estimate the external magnetic field using a modified Tsyganenko 96 (T96) magnetospheric magnetic field model (Tsyganenko, 1995, 1996), developed for the terrestrial magnetosphere, driven using solar wind and IMF data from the Advanced Composition Explorer (ACE), scaled to the appropriate Mercury-orbit heliocentric distance. This scheme provides an estimate of the expected magnitude and variability in the external field. This synthetic data set is used as input to dipole and multipole inversion procedures.We consider an internal magnetic field consisting of dipole and quadrupole terms, which allows us to quantify the expected error in the recovery of these terms and to specify the degree to which they may be independently determined. The results show that the MESSENGER data set should allow identification of higher-order terms contributing more than a few percent to the total surface field. We discuss the technical approach of the multipole inversion in Section 2. The simulation of Mercury's external magnetic field and its consideration in the inversion process are illustrated in Sections 3 and 4, respectively. The inversion results are then presented in Section 5 and subsequently discussed in Section 6. Finally, we summarize the results in Section 7.

2. Multipole inversion

Mercury's intrinsic magnetic field can be determined from the magnetic field observations obtained during the orbital phase of the MESSENGER mission by spherical harmonic analysis. A technique similar to the one used here has been applied to Pioneer 11 magnetic field data at Jupiter by Connerney (1981). The technique is based on the assumption that the data were obtained in a source-free region of space, such that $\nabla \times \underline{B} = 0$. The magnetic field $\underline{B}$ can then be expressed as the gradient of a scalar potential function:

$$\underline{B} = -\nabla\psi \tag{1}$$

which can be represented by a spherical harmonic expansion series for the internal field:

$$\psi = R_{\mathrm{M}} \sum_{l=1}^{\infty} \left(\frac{R_{\mathrm{M}}}{r}\right)^{l+1} \times \sum_{m=0}^{l} (g_l^m \cos m\lambda + h_l^m \sin m\lambda) P_l^m(\cos\theta). \tag{2}$$

In (2) the P_l^m are the Schmidt-normalized associated Legendre polynomials, and the g_l^m and h_l^m are the spherical harmonic coefficients describing the multipole configuration of the magnetic field. For a number of magnetic field measurements Eqs. (1) form a system of linear equations

$$\underline{\underline{A}}\,\underline{m} = \underline{d}, \tag{3}$$

where the matrix $\underline{\underline{A}}$ contains the derivatives of the spherical harmonic expansion of the potential function corresponding to the three magnetic field components, the data vector $\underline{d}$ consists of the magnetic field observations, and $\underline{m} = (g_l^m, h_l^m)^{\mathrm{T}}$ is the unknown model vector. The least-squared solution of a system of linear equations (3) is conveniently found using singular value decomposition (SVD) (Lanczos, 1958), which allows any matrix $\underline{\underline{A}}$ to be decomposed into a product of matrices

$$\underline{\underline{A}} = \underline{\underline{U}}\,\underline{\underline{\Lambda}}\,\underline{\underline{V}}^{\mathrm{T}}, \tag{4}$$

where $\underline{\underline{U}}$ and $\underline{\underline{V}}$ are orthogonal matrices and $\underline{\underline{\Lambda}}$ is a diagonal matrix containing positive or zero elements, the singular values. Constructing the pseudo inverse $\underline{\underline{A}}^{+} = \underline{\underline{V}}\,\underline{\underline{\Lambda}}^{-1}\,\underline{\underline{U}}^{\mathrm{T}}$, the model vector $\underline{m}$ is given by

$$\underline{m} = \underline{\underline{V}}\,\underline{\underline{\Lambda}}^{-1}\,\underline{\underline{U}}^{\mathrm{T}}\underline{d}. \tag{5}$$

The error margins of the model parameters can be determined by analyzing the model covariance matrix (Menke, 1984)

$$\mathrm{cov}(\underline{m}) = \underline{\underline{A}}^{+}\mathrm{cov}(\underline{d})(\underline{\underline{A}}^{+})^{\mathrm{T}}. \tag{6}$$

If the data are uncorrelated, the data covariance matrix $\mathrm{cov}(\underline{d})$ is a diagonal matrix, whose elements are the variances σ_{d}^2 of the data. Assuming that all these variances are identical, the model covariance matrix becomes

$$\mathrm{cov}(\underline{m}) = \sigma_{\mathrm{d}}^2 \underline{\underline{A}}^{+}(\underline{\underline{A}}^{+})^{\mathrm{T}} = \sigma_{\mathrm{d}}^2 \underline{\underline{V}}\,\underline{\underline{\Lambda}}^{-2}\underline{\underline{V}}^{\mathrm{T}}. \tag{7}$$

Under the assumption that all uncertainties are instrumental, the variance σ_{d}^2 can be estimated from the data (Bevington, 1969):

$$\sigma_{\mathrm{d}}^2 \approx \frac{1}{N_{\mathrm{d}} - N_{\mathrm{m}}} (\underline{d} - \underline{\underline{A}}\,\underline{m})^2, \tag{8}$$

where N_{d} is the number of data points and N_{m} is the number of model parameters. Substituting (8) into (7), the statistical errors of the spherical harmonic coefficients g_l^m and h_l^m are given by the diagonal elements of the model covariance matrix

$$\sigma_{\mathrm{m},j} = \sqrt{\mathrm{cov}(m_{jj})}. \tag{9}$$

It is important to note that the statistical errors in (9) provide no information about systematic errors.

The off-diagonal elements of the model covariance matrix provide additional information about the dependence of two model parameters on each other via the correlation coefficient

$$r_{ij} = \frac{\mathrm{cov}(m_{ij})}{\sigma_{\mathrm{m},i}\sigma_{\mathrm{m},j}}, \tag{10}$$

which ranges between -1 and $+1$. Ideally, all model parameters are uncorrelated, and the correlation coefficients are thus zero. In reality the spatial density and distribution of observations give rise to correlation between distinct model parameters to a greater or lesser extent. The correlation coefficient is a useful measure of the independence of the dipole and quadrupole terms in the inversion. It depends only on the data kernel and the covariance of the data, not on the data itself, as can be seen from (7) and (9).

3. Magnetic field simulation

3.1. External field model

The basis of our analysis is a simulated set of magnetic field observations along the MESSENGER trajectory in orbit around Mercury. The magnetic field model implemented in the simulation consists of a Mercury internal dipole source and an external contribution described by a modified Tsyganenko 96 model. The T96 external field is a semi-empirical magnetic field model of the Earth's magnetosphere, established by fitting a multitude of observations, parameterized by various conditions of the solar wind and the IMF, to the magnetic fields associated with the most dominant terrestrial current systems, including the magnetopause current, the tail current, Birkeland currents, and the ring current. Although these sources of the model field are not specific to the terrestrial magnetosphere, we retained only the magnetopause and tail currents in our simulation of Mercury's external field. Charged particles in Mercury's magnetosphere do not trace out complete drift shells, so that a ring current, as it is known in the terrestrial magnetosphere, does not exist at Mercury, and the associated magnetic field in the T96 model is set to zero. Slavin et al. (1997) attribute features in the Mariner 10 data to field-aligned currents, so it is possible that a Birkeland current system exists at Mercury and will need to be considered. At present however, we also omit the magnetic field of the field-aligned currents, because we expect the conditions in Mercury's magnetosphere to be quite different from those at Earth, owing to the absence of a conducting ionosphere.

The output of the T96 model is a magnetic field vector, whose components depend on the position in the Earth's magnetosphere, the ring current, the planetary tilt angle, as well as the solar wind dynamic pressure and the B_y- and B_z-components of the IMF. The scaling of the model to Mercury's magnetosphere requires adjusting several input parameters. Since the equatorial magnetic field strength at Mercury $B_{eq,M}$ is only a fraction of that of the Earth $B_{eq,E}$, all MESSENGER trajectory coordinates, given in units of Mercury radii (R_M), have to be scaled to Earth radii (R_E) in such a way that the equatorial field strengths in both planetary systems are equal. The suitable linear scaling factor between the two magnetospheres is thus $(B_{eq,E}/B_{eq,M})^{1/3}$, with $B_{eq,E} = 30574$ nT. That is, if $B_{eq,M} = 300$ nT, then a radial distance of 8 R_E in the T96 model corresponds to 1.7 R_M in our simulation. The T96 ring current is set to zero at all times, corresponding to the absence of closed drift paths, as discussed above. Furthermore, we assume that Mercury's dipole axis is aligned with the planetary rotation axis, establishing a tilt angle of 0°.

It should be noted that the external field model does not capture the magnetospheric dynamics, e.g., magnetic substorms, and the scaling of solar wind observations at Earth to Mercury orbit does not account for the evolution of Alfvénic fluctuations, shocks, or stream interaction regions between 0.3 and 1.0 AU. Moreover, the present magnetic field model does not yet consider the magnetic field due to currents induced in the planetary interior by variations in solar wind pressure, which may contribute up to 15% to the magnitude of the intrinsic magnetic field (Glassmeier, 2000).

3.2. Interplanetary solar wind conditions

The solar wind data used to drive the model are taken from the database of the Level 2 data from the MAG (Smith et al., 1998) and SWEPAM (McComas et al., 1998) instruments on the ACE spacecraft. The ACE data set was chosen because it provides a full year of continuous data in a solar cycle phase (1998) comparable to that to be seen by MESSENGER (2009–2010). The measurements are scaled from the ACE location at 1 AU to Mercury distances using the Parker solar wind solution (e.g., Parks, 1991):

$$\left(\frac{U^2}{C_s^2} - 1\right)\frac{dU}{U} = \left(2 - \frac{GM}{C_s^2 r}\right)\frac{dr}{r}, \tag{11}$$

where U is the fluid speed, C_s is the speed of sound in a gas, G is the gravitational constant, M is the mass of the Sun, and r is the heliocentric distance. Assuming that C_s is constant and imposing the boundary condition that $U = C_s$ when $r = r_c$, the solution to the differential equation (11) is

$$\frac{U^2}{C_s^2} - 2\ln\left(\frac{U}{C_s}\right) = 4\ln\left(\frac{r}{r_c}\right) + 4\left(\frac{r_c}{r}\right) - 3 \tag{12}$$

with $r_c = GM/(2C_s^2)$. Eq. (12) is used to determine the flow speed ratio between ACE and Mercury heliocentric distances. The solar wind speed at Mercury is then modelled as the speed measured at ACE adjusted by this ratio. At Mercury distances between 0.31 and 0.47 AU the solution of (12) may be approximated by the second-order polynomial

$$U_M = 11.06 + 201.04r - 140.11r^2, \tag{13}$$

where $C_s = 39$ km/s has been assumed.

Eq. (13) can be used together with the solution of (12) for the ACE location at 1 AU, $U_E = 98.67$ km/s, to scale the solar wind speed $v_{p,E}$, as measured by the ACE spacecraft, to Mercury:

$$v_{p,M} = v_{p,E}\frac{U_M}{U_E}, \tag{14}$$

where the subscripts M and E refer to Mercury and Earth, respectively. The scaling in (14) accounts for the effects of variations in C_s on $v_{p,E}$, but the scaling ratio, which is not a sensitive function of C_s, is fixed.

The equivalent scaling for the solar wind density n_p can be obtained from the continuity equation, $n_p v_p r^2 = \text{constant}$, since the number of particles traversing through any two spheres concentric to the Sun must be equal. Using (14) yields

$$n_{p,M} = n_{p,E}\left(\frac{r_E}{r_M}\right)^2\frac{U_E}{U_M}. \tag{15}$$

The solar wind dynamic pressure required to drive the T96 model can then be derived from (14) and (15):

$$p_{\mathrm{dyn,M}} = m_{\mathrm{p}} n_{\mathrm{p,M}} v_{\mathrm{p,M}}^2, \tag{16}$$

where m_{p} is the proton mass. Solar wind composition effects are ignored, because they amount only to about a 10% correction to $p_{\mathrm{dyn,M}}$.

The IMF measurements can be similarly scaled to the Mercury distance range. Using the streamline equation (e.g., Parks, 1991), one obtains the radial dependence of the radial and azimuthal IMF components as

$$B_{\mathrm{r}}(r) = B_{\mathrm{r}}(r_{\mathrm{c}}) \left(\frac{r_{\mathrm{c}}}{r}\right)^2, \tag{17}$$

$$B_{\phi}(r) = B_{\mathrm{r}}(r_{\mathrm{c}}) \left(\frac{r_{\mathrm{c}}}{r}\right)^2 \frac{\Omega(r - r_{\mathrm{c}})}{U}, \tag{18}$$

where the Sun rotates with the angular velocity Ω. The IMF data measured by ACE are then scaled to Mercury by comparison between the two locations of interest:

$$B_{\mathrm{r}}(r_{\mathrm{M}}) = B_{\mathrm{r}}(r_{\mathrm{E}}) \left(\frac{r_{\mathrm{E}}}{r_{\mathrm{M}}}\right)^2, \tag{19}$$

$$B_{\phi}(r_{\mathrm{M}}) = B_{\phi}(r_{\mathrm{E}}) \left(\frac{r_{\mathrm{M}} - r_{\mathrm{c}}}{r_{\mathrm{E}} - r_{\mathrm{c}}}\right) \left(\frac{r_{\mathrm{E}}}{r_{\mathrm{M}}}\right)^2, \tag{20}$$

$$B_{\theta}(r_{\mathrm{M}}) = B_{\theta}(r_{\mathrm{E}}) \left(\frac{r_{\mathrm{M}} - r_{\mathrm{c}}}{r_{\mathrm{E}} - r_{\mathrm{c}}}\right) \left(\frac{r_{\mathrm{E}}}{r_{\mathrm{M}}}\right)^2. \tag{21}$$

Because the streamline equation does not include any information about the radial dependence of the polar IMF component B_{θ}, we adopt (20) for the B_{θ}-component of the IMF (Slavin and Holzer, 1979).

The suitability of the IMF scaling can be tested by comparing the scaled ACE magnetic field data with measurements taken by the HELIOS spacecraft in the heliocentric distance range of Mercury's orbit. Fig. 1 shows the occurrence rates of 1-h averages of the three IMF components in the HELIOS and scaled ACE data sets. The HELIOS statistics are compiled from measurements obtained during the years 1975 through 1981, whereas the statistical ACE data include only the time range from April 10, 1998, to April 10, 1999. The time interval for the ACE data was selected to be in approximately the same phase of the solar cycle as the orbiting phase of the MESSENGER mission. Note that the 1-h statistics of the ACE data presented in Fig. 1 are used only for comparison with the HELIOS observations. The time resolution employed for driving the T96 model is much higher. The x-direction in Fig. 1 points toward the Sun, z is perpendicular to the ecliptic plane, and y completes the right-handed coordinate system. The departure of the Sun's spin axis from the ecliptic normal of about 7° has been ignored. This coordinate system is similar to the GSE system used in terrestrial magnetospheric physics.

The two statistical data sets are generally in good agreement with each other, validating the scaling procedure discussed above for representing the statistical distribution of

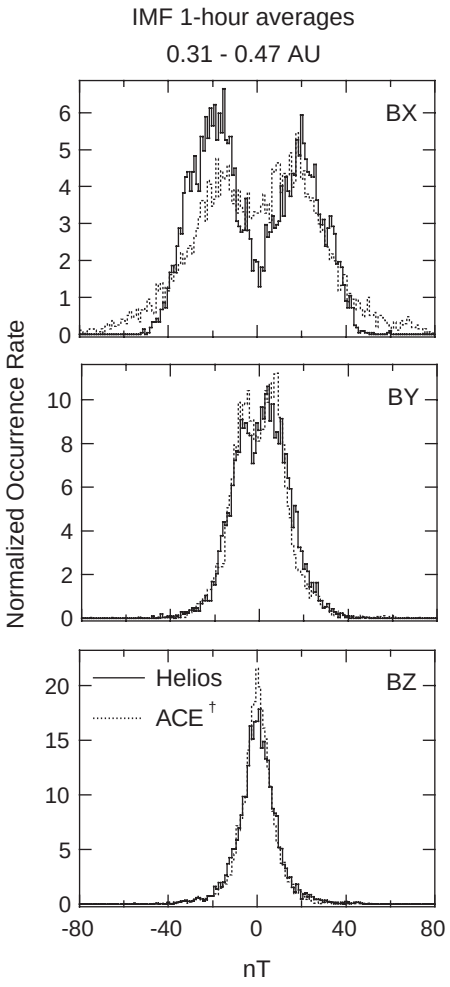

Fig. 1. Normalized occurrence rate of the three components of the IMF between 0.31 and 0.47 AU. The solid lines represent the HELIOS statistics compiled from 6 years of data between 1975 and 1981. The dotted lines show the scaled ACE data, indicated by the † symbol in the legend.

the IMF environment at Mercury. The histograms of the B_x-components show the largest differences. The HELIOS distribution is more bimodal than the ACE statistics, a difference attributed to a higher level of fluctuations, relative to the average absolute value, in the radial component at the Lagrange point L1 than at Mercury orbit distances. At Mercury, B_{r} is the dominant IMF component and Alfvénic fluctuations are comparatively small, so that the B_x-distribution is more clearly bimodal than in our scaled data set. Since the Mercury external field model we are using here depends only on B_y and B_z, differences in the B_x-distribution are not relevant for the purpose of driving the external field model. The B_x-distribution is potentially of great importance for the actual dynamics of Mercury's magnetosphere, however, since the dominance of B_x at Mercury implies that the subsolar bow shock is most often quasi-parallel, i.e., the subsolar shock normal and the magnetic field are parallel, which implies that the bow shock at Mercury is likely to be more inherently dynamic than it is at Earth (Russell et al., 1988).

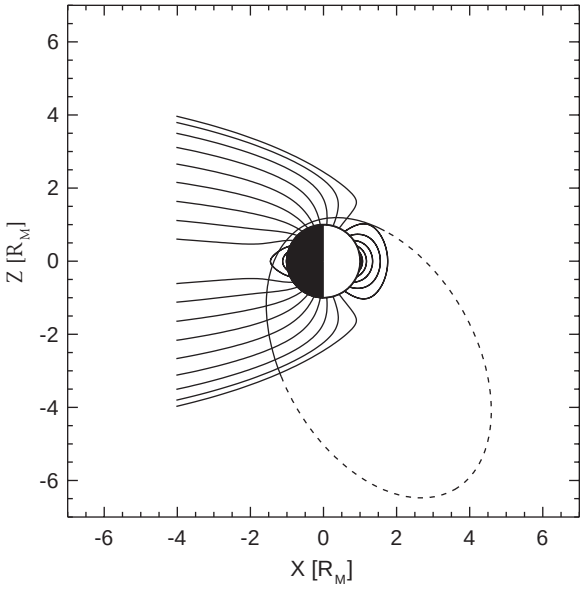

Fig. 2. MESSENGER noon-midnight orbit on April 17, 2009, with periherm on the nightside at 260 km altitude and 60°N latitude. Along the orbit, the spacecraft passes through regions of magnetospheric (solid line) and solar wind (dotted line) field lines. Magnetospheric field lines are superimposed on the plot.

3.3. Simulated external field contribution

To simulate the effects of the solar wind and IMF and their variability on the MESSENGER magnetic field observations, we use the 1-year time series of ACE data as a time-variable input to the T96 model and evaluate the net magnetic field in 1-min time steps along the MESSENGER orbit trajectory. For this purpose, the IMF and solar wind data are interpolated and scaled from 4-min averages of the ACE/MAG database and 64-s averages of the ACE/SWEPAM observations, respectively. The field-line topology (magnetospheric, solar wind) was determined by tracing the field lines. Fig. 2 shows the MESSENGER trajectory for a noon-midnight orbit together with a set of magnetic field lines, indicating the size of Mercury's magnetosphere. The x-direction is positive toward the Sun, z is normal to Mercury's orbit plane, and y is positive toward dusk.

The external contribution to the magnetic field given by the T96 model along a typical pass of the MESSENGER spacecraft through Mercury's magnetosphere is shown in the bottom panel of Fig. 3. The ratio of the external contribution to the internal field (middle panel of Fig. 3), calculated for a dipole strength of 300 nTR_M^3, indicates that the external magnetic field strength (solid line, bottom panel) represents a considerable contribution to the total field. The key features of the MESSENGER observations we seek to simulate are the significant time variations and orbit-to-orbit variability of the external magnetic field strength that we expect due to the fluctuations in the solar wind and the IMF. An example of the variability in the total external field intensity B_{T96} is shown in Fig. 4 for five consecutive magnetosphere passes.

Differences among magnetosphere passes are associated with differences in the scaled IMF and solar wind dynamic pressure. Simulated variations between orbits and during an orbit range up to 100 nT or larger, consistent with the large variations observed during the Mariner 10 encounter I (Ness et al., 1974).

4. External field correction

As noted in Section 3, an accurate determination of Mercury's intrinsic magnetic field requires proper correction for the external field contribution. This correction can be accomplished by modifying (5):

$$\underline{m} = \underline{\underline{V}}\,\underline{\underline{\Lambda}}^{-1}\,\underline{\underline{U}}^{\mathrm{T}}(\underline{d}_{\mathrm{obs}} - \underline{d}_{\mathrm{ext}}), \tag{22}$$

where the vector $\underline{d}_{\mathrm{obs}}$ contains the magnetic field observations and the $\underline{d}_{\mathrm{ext}}$ are estimates of the external field. This correction also satisfies the condition $\nabla \times \underline{B} = 0$ in an average sense. Clearly, for $\underline{d}_{\mathrm{ext}}$ we do not simply subtract the external field contribution, but rather we assess the solar wind and IMF inputs for the external field estimate directly from the simulated data. The solar wind pressure is estimated from magnetopause crossings, and the IMF is evaluated from the period of solar wind observations just prior to each pass through the magnetosphere.

An average dynamic pressure, to be used for the entire time period of the inversion, is derived from a model magnetopause best-fit to magnetopause crossings identified in the simulated data. The detailed procedure is as follows. The coordinates of magnetopause crossings observed in the data are scaled to Earth with the zero-order estimate for $B_{\mathrm{eq,M}}$ recovered by (5). A prolate ellipsoid,

$$ax^2 + bx + c + y^2 + z^2 = 0, \tag{23}$$

is then fit to the scaled magnetopause crossings, establishing the lengths of the semi-major axes a, b, and c in a least-squared sense. Setting $y = z = 0$, the magnetopause stand-off distance r_s yields

$$r_s = -\frac{b}{2a} \pm \sqrt{\left(\frac{b}{2a}\right)^2 - \frac{c}{a}}. \tag{24}$$

Choosing the sign of the square root appropriately (i.e., to give the smaller root), the solar wind dynamic pressure can then be derived from the stand-off distance as

$$p = p_0 \left(\frac{r_s}{r_{s0}}\right)^{-6} \tag{25}$$

with $p_0 = 2.04$ nPa and $r_{s0} = 11.08\ R_E$ (Sibeck et al., 1991; Tsyganenko, 1995). The resulting pressure p is used in the T96 model for the entire time period to estimate $\underline{d}_{\mathrm{ext}}$.

The IMF parameters driving the T96 model are determined from separate statistics for each orbit. Because the

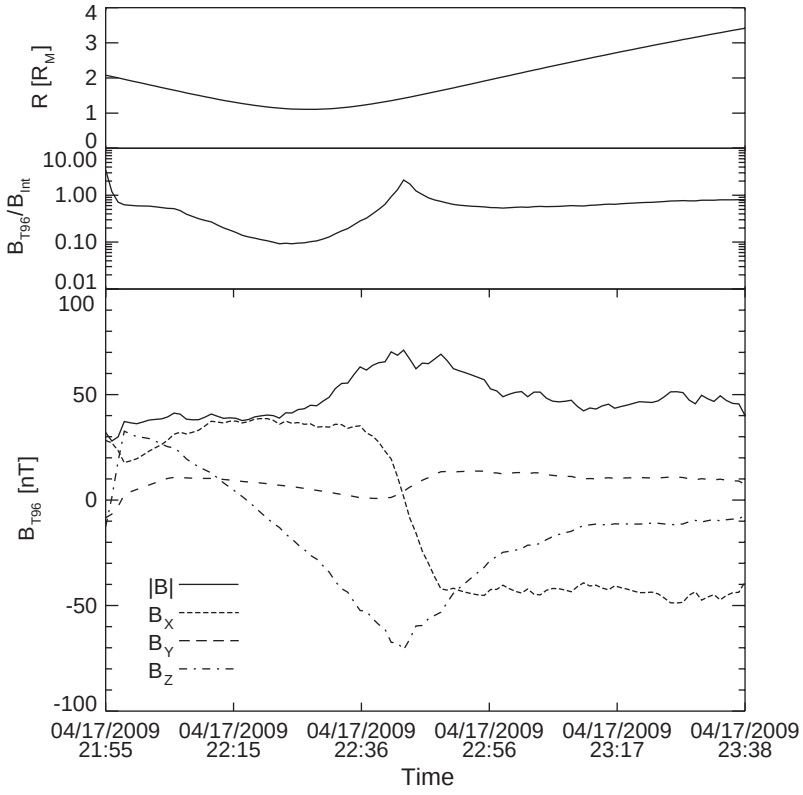

Fig. 3. Contribution of the external magnetic field along the spacecraft trajectory during one magnetosphere pass calculated with the T96 magnetic field model scaled to Mercury (bottom panel). The top and middle panels show the radial distance of the spacecraft from Mercury and the ratio of the external to the internal field contributions, respectively.

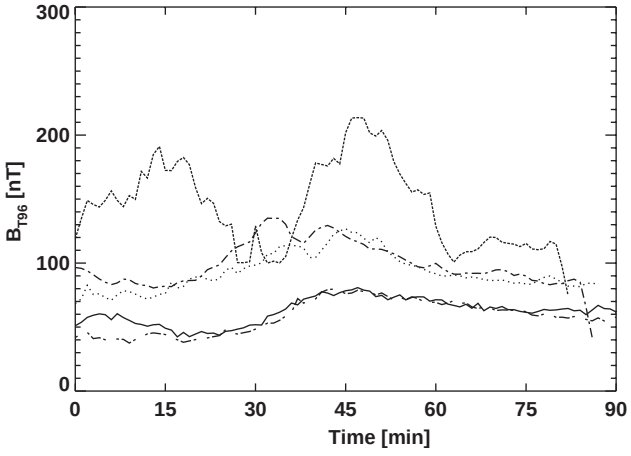

Fig. 4. Example of orbit-to-orbit variations of the T96 external magnetic field strength B_{T96}, shown for five consecutive MESSENGER passes through Mercury's magnetosphere as a function of time elapsed in each orbit after the inbound magnetopause crossing.

overall average of the IMF is zero whereas the average external field is not, the following procedure was used to obtain an average external field. For a given magnetosphere pass, the magnetic field data of the preceding solar wind part of the orbit are sorted into 60°-wide bins in the y–z-plane. The angle in the y–z plane, called the clock angle, is measured with reference to the $+z$-direction, with $+90°$ toward $+y$. The average IMF is calculated in each of the six IMF clock angle bins (0°, ±60°, ±120°, 180°). For every observation in the magnetosphere, the T96 model is evaluated using the average IMF in each clock angle bin, and the total external field contribution is the average of these six values, weighted by the number of IMF measurements in each bin.

The results obtained by determining the external magnetic field contribution in this manner represent optimal conditions. Although we have evaluated the input parameters to the external field correction from the simulated observations, the transfer function between the inputs and the external field, the T96 model, is precisely what we used to create the simulated data set. Our results therefore provide a best-case benchmark for the information that one may extract from the MESSENGER observations.

5. Results

5.1. Application to Mariner 10

The performance of the inversion algorithm without external field correction is verified by application to Mariner 10

magnetic field data from the Mercury encounters I and III. Assuming that Mercury's intrinsic magnetic field is an axial centered dipole configuration, a dipole moment of 287 ± 13 nTR_M^3 is obtained from this data set, where the error indicated is the standard deviation in (9). In the approximation that the internal field can be represented as a centered dipole plus a centered quadrupole, the quadrupole is 122 ± 16 nTR_M^4 while the dipole is reduced to 210 ± 15 nTR_M^3. However, the dipole-plus-quadrupole solution is non-unique, and the higher-order term can also be attributed to an off-centered dipole position. In order to demonstrate this equivalency, we relax the constraint on the location of the magnetic moment and determine dipole moment and offset in an iterative approach by shifting the dipole's position. Minimizing the residual field vector between observations and model results in a dipole moment of 201 ± 5 nTR_M^4 with an offset of $x = +0.01R_M$, $y = +0.02R_M$, and $z = +0.20R_M$. Ignoring the comparatively small offsets in x and y, one obtains for a small displacement of an axis-aligned dipole along its axis z (Chapman and Bartels, 1940):

$$g_2^0 \approx 2\Delta z g_1^0, \tag{26}$$

where g_1^0 and g_2^0 are the dipole and quadrupole components, respectively, and Δz is the displacement in units of planetary radii. By Eq. (26) the above offset location of $0.2R_M$ in $+z$-direction is interchangeable with a quadrupole coefficient of $g_2^0 = 115$ nT. This result agrees reasonably well with the quadrupole term of $g_2^0 = 122$ nT obtained from the centered dipole-plus-quadrupole configuration and is thus an alternative interpretation to the coefficients obtained from inversion of the Mariner 10 observations.

The impact of the external field can be demonstrated by considering the minimum and maximum T96 model field as two extreme conditions, representing a very quiet and a greatly disturbed magnetosphere, respectively. The largest model fields are obtained for high solar wind dynamic pressures and a strong, southward-oriented IMF. On the other hand, weak solar wind pressures and a northward orientation of the IMF result in smaller external field contributions. The Mariner 10 solar wind data as well as the HELIOS and ACE statistics in Fig. 1 indicate that an IMF $B_z = \pm 30$ nT characterizes these conditions reasonably well. Solar wind dynamic pressures of 4.9 nPa for a quiet magnetosphere and 15.2 nPa for active periods were obtained as extremal values by applying (16) to the statistics of the ACE particle data. The external magnetic field, evaluated by the T96 model driven by the solar wind parameters established above, is then subtracted from the Mariner 10 magnetic field observations prior to inversion. The resulting strength of the dipole moment ranges between 198 nTR_M^3 and 348 nTR_M^3, consistent with findings from various authors, summarized by Lepping et al. (1979), as well as more recent modeling results by Engle (1997). Therefore, we conclude that uncertainties in the determination of the dipole strength are largely due to the uncertainty of the external field contribution. Because the Mariner 10 magnetopause crossings were close to the flanks of the magnetosphere, the subsolar standoff distance is poorly constrained, with the result that the correction of the external field as described in Section 4 is inapplicable to the Mariner 10 data.

5.2. Simulated MESSENGER observations

The inversion algorithm was applied to magnetic field data simulated along the MESSENGER trajectory by the procedure described in Section 3. The intrinsic field was simulated using a centered dipole aligned with the planet's rotation axis. Since there is a large uncertainty in Mercury's magnetic dipole moment, a range of potential planetary magnetic moments between 100 nTR_M^3 and 500 nTR_M^3 was considered. The differences between the moment and position obtained from the inversion and the input dipole are illustrated in Fig. 5 as functions of the input planetary magnetic moment from the first month of the orbital mission phase. Because Mercury's rotation period is 58.6 days, the longitude of periapsis of the MESSENGER orbit will have moved by more than 180° over this time interval. Figs. 5a and b show the error in the moment as a percentage of actual moment used in the simulation for the centered and offset dipole inversions, respectively. The inversion for the offset dipole is by the same technique as for the centered dipole, except that the dipole location is a free parameter determined by iteratively moving the position to minimize the residuals. Any deviation of the dipole location from the origin is an error in the position, and we define the norm of the offset vector as the position error (Fig. 5c). The error in the solution at a given planetary moment is determined largely by the magnitude of the external field strength. To illustrate the range of moment solutions that could be obtained, the lower and upper error estimates (dashed and dotted curves in Fig. 5) are inferred by adopting the extreme solar wind conditions used to generate the external field contributions for the Mariner 10 flybys in Section 5.1. Driving the T96 model with the continuous stream of scaled ACE data described above gives the error estimates shown by solid lines in Fig. 5.

Since the contribution of the external magnetic field to the total field decreases with increasing strength of the intrinsic field, the errors in Fig. 5 are larger for smaller planetary magnetic moments. In the worst case for the centered dipole (Fig. 5a) we find that the error for small planetary moments can reach values as great as 50%, but it may be as low as 7% for an intrinsic moment of 500 nTR_M^3. Inversions of magnetic field simulations using scaled ACE solar wind data to drive the external field show that planetary moment can be determined within 5% of its actual value for a dipole strength of around 300 nTR_M^3. Uncertainties in the position of the planetary moment increase the error in the magnitude of the moment strength, as shown in Fig. 5b. For intrinsic magnetic fields less than 100 nT at the equator, the accuracy in the magnitude of the moment would be no better

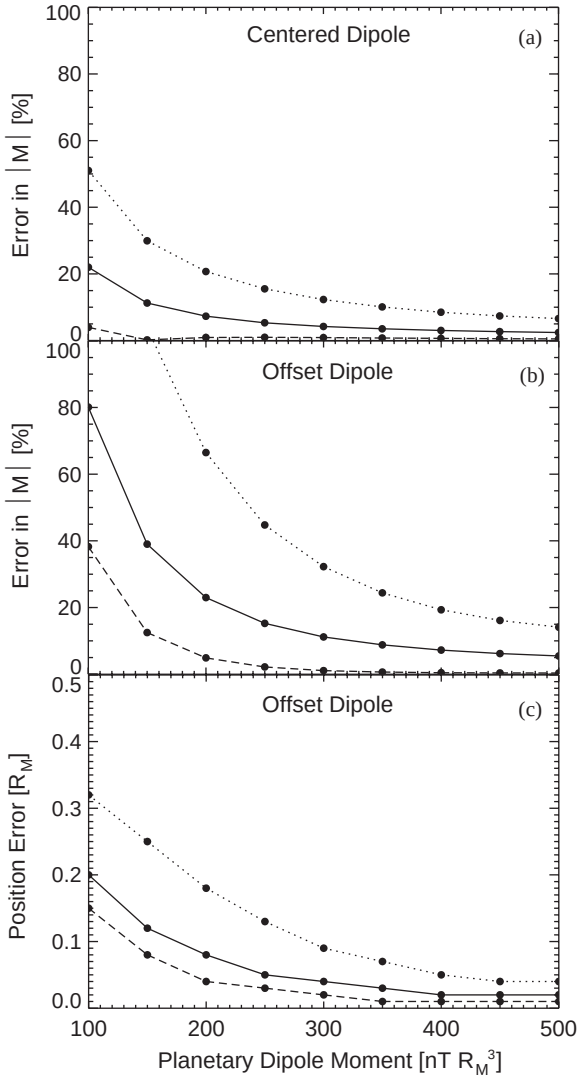

Fig. 5. Errors in dipole characteristics as functions of planetary moment for the (a) centered- and (b, c) offset-dipole models using 1 month of simulated MESSENGER magnetic field observations. The dashed and dotted curves depict errors obtained from the simulated data sets with the smallest and largest estimated external field contribution, respectively, while the solid curve corresponds to an external field contribution acquired by driving the T96 model with scaled ACE data. The error in offset of a dipole allowed to vary in position is shown in (c).

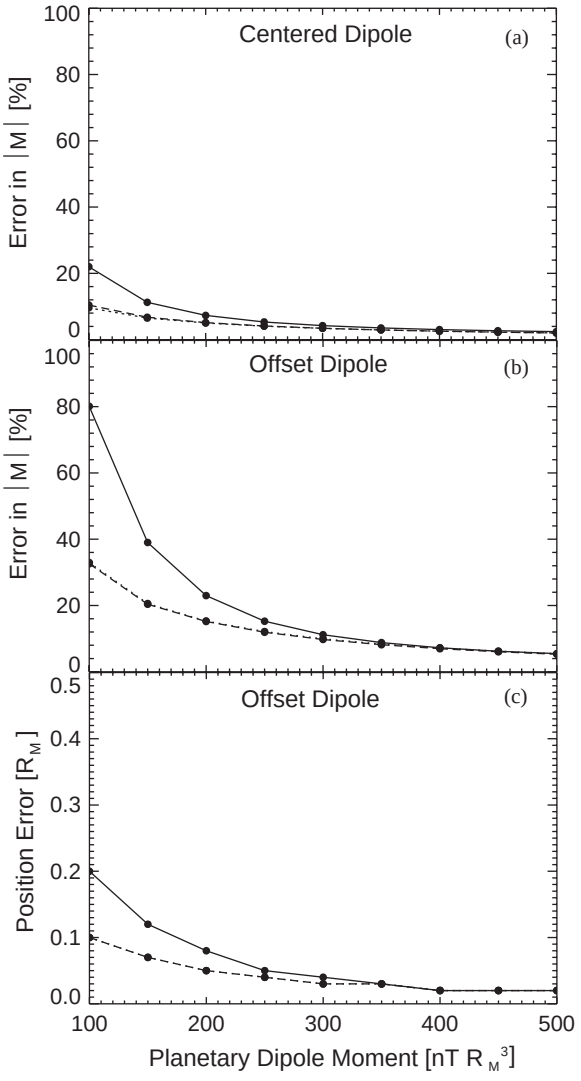

Fig. 6. Errors in dipole characteristics as functions of planetary moment for the (a) centered- and (b, c) offset-dipole models using 1 month (solid lines), 3 months (dashed lines), and 12 months (dotted lines) of simulated MESSENGER magnetic field observations. The error in offset of a dipole allowed to vary in position is shown in (c). The dashed and dotted lines coincide in all three panels.

than a factor of 2, and the actual position may deviate more than $0.3R_M$ from the inversion solution. However, if Mercury's magnetic moment is nearly consistent with previous findings, we anticipate errors in the dipole strength of about 10% and about $0.05R_M$ in its position using one month of observations.

The accuracy to which Mercury's intrinsic moment can be determined depends on the statistics of the observations, on the distribution of the measurements, and on the knowledge of the external magnetic field. As the orbital phase of the mission advances, the planetary coverage of the observations increases while the statistics are simultaneously enhanced. The growing data set initially reduces the error, as illustrated in Fig. 6, which depicts results of inversions of simulated magnetic field data 1 month (solid lines), 3 months (dashed lines), and 12 months (dotted lines) after orbit insertion. The external field model is driven by the scaled ACE solar wind data, so the solid curves in Figs. 5 and 6 are identical. The plot format is adopted from Fig. 5, showing the centered dipole evaluation in Fig. 6a and the error estimates for the moment and position of the offset dipole in Figs. 6b and c, respectively. From Fig. 6 it is evident that inversions of small planetary moments benefit significantly from the larger data accumulation interval. The error estimates for the centered dipole at 100 nTR_M^3 moment drop with an additional 2 months of data by approximately

a factor of 2, reaching the 10% level after three months. For the offset dipole, the error in the magnetic moment at 100 nTR_M^3 is likewise considerably reduced from 80% after 1 month to 33% after 3 months, and the position uncertainty is lowered from $0.2R_M$ to $0.1R_M$. The correlation between the dipole and quadrupole terms, obtained from (10), ranges from −0.84 to −0.86, depending on the number of observations included in the inversion.

The error estimates for small planetary moments improve noticeably during the first 3 months of the MESSENGER orbital phase, but only minimal improvements are achieved for intrinsic moments above 300 nTR_M^3 beyond the first month. This indicates that the remaining errors are systematic rather than random. As Fig. 6 illustrates, increasing the number and coverage of the measurement points does not by itself indefinitely reduce the error of the inversion. Although the statistical errors do decrease as the data set grows, they are of secondary concern because their magnitudes are smaller than the systematical errors we obtain. The leading causes for systematic errors in our calculations are the orbital bias of the observations, being below 1000 km altitude only in the northern hemisphere, and the fact that the external field is not a linear function of the solar wind dynamic pressure, whereas we have taken a mean magnetopause position to define an average pressure. Improvements in the specification of the solar wind conditions may help to reduce the errors, but the results also indicate that the accuracy of the external model will be critical. Since the MESSENGER data will be used to refine the external magnetic field model it will be very important to use the entire 12 months of observations to make the external field model as accurate as possible.

When corrections for the external field are applied, the systematic errors are reduced considerably. This result is shown in Fig. 7, where the external field correction is applied to the entire 12-month interval of the ACE-driven MESSENGER magnetic field simulation, as described in Section 4. The plot format is identical to Figs. 5 and 6, and the uncorrected curves (dotted lines in Fig. 7) are taken from Fig. 6 for comparison. With the external field correction, the error estimates for the planetary moment (Figs. 7a and b) are generally less than half that without the correction. Furthermore, the dipole location (Fig. 7c) is determined to within a few tens of kilometers after subtraction of the external field contribution. Similar inversions with correction for the external field were done using the 3-month data set as well, and the systematic errors were nearly identical to those obtained from inverting the 12-month data set, consistent with the above results for the dipole inversion.

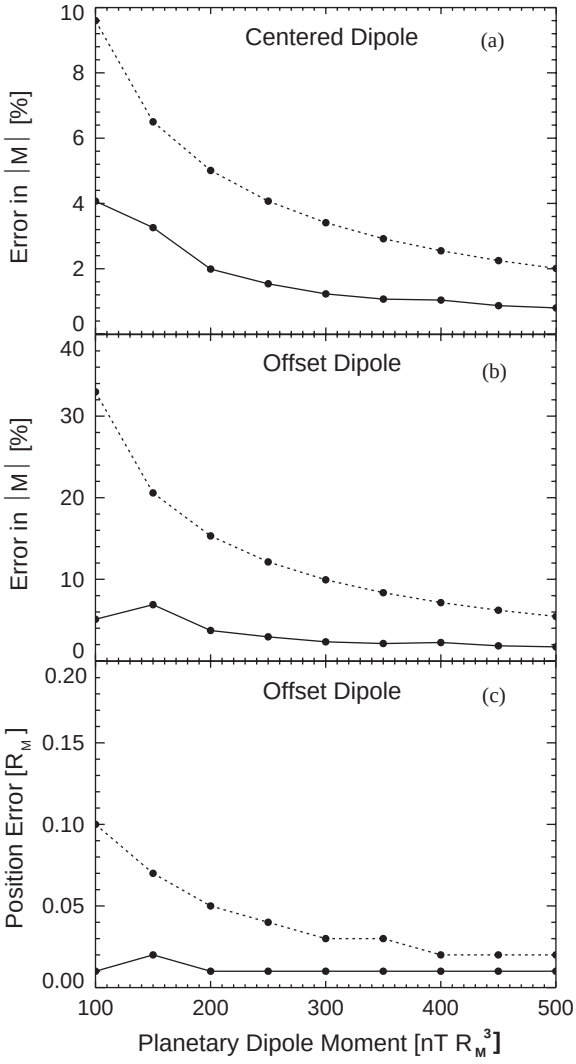

Fig. 7. Errors in dipole characteristics as functions of planetary moment for the (a) centered- and (b, c) offset-dipole models using 12 months of simulated MESSENGER magnetic field observations. The inversions represented by the solid lines have been corrected for the external field contribution, while the dotted lines represent results obtained from uncorrected observations. The error in offset of a dipole allowed to vary in position is shown in (c).

5.3. Higher-order terms

The dipole term of the magnetic field is fundamental to understanding Mercury's magnetosphere, but accurate knowledge of the dipole is important only in so far as it allows identification of higher-order terms, because only the structure of the field can help distinguish between theories for sources and origins of the planetary field. It is crucial therefore to consider the errors present in higher-order terms. The inversion technique described in Section 2 provides the spherical harmonic coefficients to an arbitrary degree of sophistication, but they are subject to significant systematic errors, because the external field contribution leads to higher-order terms in the inversion that are unrelated to the intrinsic magnetic field of the planet.

We consider the systematic error in the quadrupole term and its reduction by use of an external field correction. Fig. 8a shows the second-order inversion solution (axial centered dipole and quadrupole) of the 12-month, 300 nTR_M^3

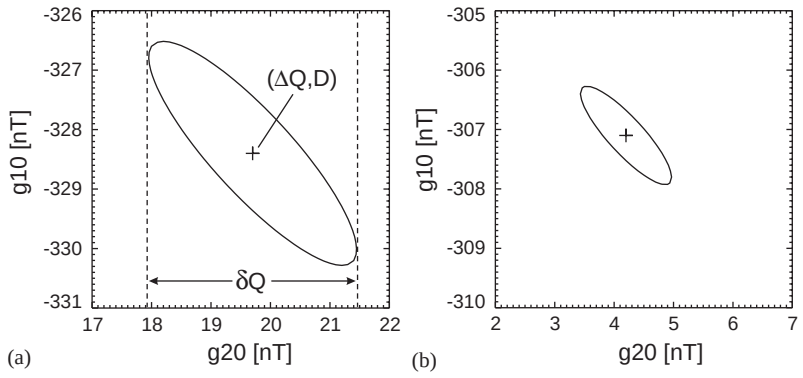

Fig. 8. Magnetic moment obtained from a second-order inversion of the 12-month, 300 nTR_M^3 data set (a) without and (b) with the external field correction applied, projected into the g_1^0–g_2^0 plane. The ellipse identifies the 3σ uncertainty level of the solution.

Table 1
Multipole inversion results without and with an external field correction assuming a purely dipolar internal field with a moment of 300 nTR_M^3. Inversions use 12 months of simulated data up to octupole

Inversion	External field correction	g_1^0 (nT)	g_2^0 (nT)	g_3^0 (nT)
Dipole (centered)	No	−310	—	—
	Yes	−304	—	—
Quadrupole	No	−329	19.8	—
	Yes	−307	4.3	—
Octupole	No	−338	41.5	−16.0
	Yes	−308	7.1	− 2.5

data set without external field correction, projected into the g_1^0–g_2^0 plane. The inversion produces an axial dipole moment of $g_1^0 = 328.5$ nT and a g_2^0 quadrupole term of 19.8 nT. The correlation coefficient between g_1^0 and g_2^0 is −0.86, which is quite high and means that errors in the dipole term correspond directly to errors in higher-order terms. Thus, for MESSENGER, the issue of dipole moment accuracy is inextricably tied to the ability to detect higher-order terms.

The width of the 3σ error ellipse shown in Fig. 8a can be interpreted as the statistical quadrupole uncertainty δQ, which amounts to 1.2% of the dipole moment. However, this error is small compared with the systematic error ΔQ due to the overall magnitude of the g_2^0 term that was not included in the forward simulation. It is caused solely by the external field contribution. If the external magnetic field is considered in the inversion, the erroneous quadrupole term is greatly reduced, and the statistical error decreases somewhat as well (Fig. 8b). The results for dipole, quadrupole, and octupole inversions are summarized in Table 1.

To be considered significant, any higher-order moment must be larger in magnitude than both the systematic error margin of the external field correction and the statistical uncertainties. The external field correction used here indicates that it should be possible to resolve terms through the octupole that contribute more than a few percent of the field at the planet's surface. The large changes that result by including the external field correction demonstrate that the determination of higher-order moments depends critically on the external field model.

6. Discussion

The results of the previous section provide an estimate of the uncertainties associated with the recovery of Mercury's magnetic field from MESSENGER observations. The key elements for a successful inversion are a large set of spatially distributed measurements and accurate correction for contamination by external fields. The dependence of the computed multipole moments on data coverage can be assessed from the correlation coefficient given by Eq. (10). Correlation between model parameters is determined by the spatial distribution of samples. To illustrate this point, consider a spherical grid of data points at constant radial distance, spaced 10° in longitude and extending from the northern planetary pole only partway to the south pole. Fig. 9 shows the correlation coefficient between the axis-aligned dipole and quadrupole terms as a function of the maximum colatitude θ_{max} of data coverage. The dipole and quadrupole contributions of the multipole field have zero systematic correlation only if data coverage is global. As the extent of the observations decreases, the model parameters become increasingly correlated. For data only from the northern hemisphere, the correlation coefficient is −0.74.

MESSENGER will supply nearly global data coverage between +80° and −70° latitude. However, because of the eccentricity and inclination of the orbit, measurements in the southern hemisphere occur at substantially higher altitudes than in the northern hemisphere, meaning that signatures of higher-order terms are effectively sampled only in the northern hemisphere. The ramifications of the altitude difference in the observations can be estimated by evaluating the correlation coefficient using the spherical grid described above,

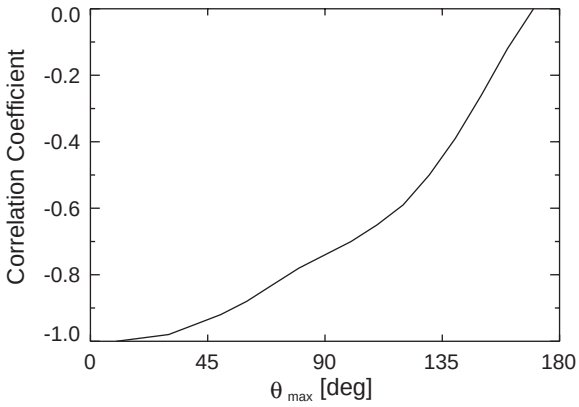

Fig. 9. Correlation coefficient between the magnetic dipole g_1^0 and quadrupole g_2^0 terms as a function of the maximum colatitude of the data coverage. Full longitudinal coverage is assumed.

but placing the data points in the northern hemisphere at $0.5R_M$ and at $1.5R_M$ altitude in the southern hemisphere. Under these conditions, even for complete global data coverage the correlation coefficient between dipole and quadrupole terms is -0.72. Therefore, the dipole-quadrupole correlation of $r \approx -0.85$ obtained above is not surprising. The high correlation implicates that extensive statistics are required to separate the g_1^0, g_2^0, and higher-order terms.

The most important source of uncertainties in obtaining the planetary moments are erroneous assumptions about the external magnetic field contribution. The need to account for external magnetic fields is emphasized by the reduction of the error (Fig. 7) and by misleading higher-order spherical harmonics (Table 1 and Section 5.3). Determining the structure of Mercury's intrinsic magnetic field therefore depends on the external field correction. The improvements obtained here are reasonable best-case estimates, since the same T96 model was used for the forward simulation and inversion. The use of the simulated data to infer an average solar wind dynamic pressure and estimated IMF for each pass introduces realistic errors. The solid curves in Fig. 7 represent the best achievable uncertainty when estimating upstream conditions as done here. The true error will approach the results obtained here as the model for the external field improves. Since the inversion technique can only be as accurate as the external magnetic field model, a detailed analysis of the magnetospheric current systems at Mercury will be crucial. Both modeling calculations of the magnetosphere and analysis of MESSENGER data for magnetospheric currents depend on knowledge of the dipole field. The fact that the dipole moment is recovered to within 10% without applying any corrections for the external field suggests that it should be possible to characterize accurately Mercury's magnetosphere based on data from MESSENGER.

In this paper we have assumed that all magnetic field observations inside Mercury's magnetosphere are included in the analysis. In reality, the magnetic field data will provide significant clues about the occurrence of dynamic magnetospheric processes, so that it will be possible to pre-select the data to be included in the inversion, so as to reduce dynamic effects to a minimum. It is expected that the most reliable solutions will be afforded by the most carefully chosen observations. The fact that the simulated inversion converges to stable results after three months of observations suggests that there is some margin for selection of optimal data without impacting the systematic errors in the inversion. We expect that the ultimate accuracy will be determined by a trade between statistical uncertainty, which grows as fewer observations are used, and systematic error, which will be reduced as the data are more carefully screened. In any case, the ultimate achievable accuracy for the dipole term may be fairly high, on the order of a few percent, and higher-order terms yielding surface fields comparable to this level should be reliably recovered.

This study focuses on the characterization of the multipole components of Mercury's magnetic field. Several complementary studies are expected to contribute to the understanding of Mercury's magnetic field. First, magnetic field observations are also planned during the two MESSENGER flybys of Mercury. These will provide the first new data on Mercury's magnetic field since the Mariner 10 observations and will be used to update our estimates of Mercury's magnetic field prior to the orbital phase of the mission. They will also be the only MESSENGER observations below 1000 km at the equator (200-km flyby closest approach). These data will likely be an important point of comparison for the inversion results. Simulation of the flyby results is not included here for several reasons. First, in comparison with the orbital data set, the flyby observations will still be a small data set. We conducted inversions that included simulated data for the MESSENGER flybys and found that their effect on the results is not statistically significant. Hence, the flyby observations need to be preferentially weighted quite strongly to affect the inversions. After the data are obtained an objective justification for preferential weighting may become apparent and could be considered at that time. Second, one could examine the set of trajectories provided by the Mariner 10 and MESSENGER flybys to assess the improvement in the statistical error (Eq. (9)) gained by adding the MESSENGER flybys to the Mariner 10 observations. The flyby data sets taken together will still be a limited set of essentially line trajectories rather a closed surface around the planet. Inversions using flyby data will therefore remain subject to significant systematic uncertainties due to the external field contribution, which will almost certainly remain larger than the statistical errors, so a measure of the improvement in the statistical uncertainty would be misleading. Finally, the systematic errors will still be too large to identify reliably quadrupole or higher-order terms. Although we could simulate the likely improvement in the dipole estimates afforded by the MESSENGER flybys, the focus of this paper is on the ultimate capability to extract higher-order terms in the intrinsic field. We have therefore restricted attention to data

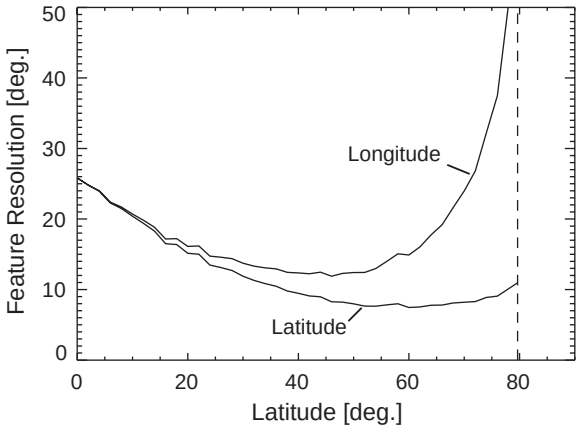

Fig. 10. Latitudinal and longitudinal feature resolution as a function of spacecraft latitude. The dashed vertical line represents the maximum latitude of the magnetic field observations.

obtained by MESSENGER during the orbital phase of the mission, in as much as these data will largely supersede the flyby data sets for the purpose of characterizing the detailed intrinsic magnetic field of the planet.

Additional analyses relate to the crustal fine structure of Mercury's magnetic field. The altitudes of the MESSENGER orbit in the northern hemisphere are sufficiently low (200-km minimum altitude) that field structures due to crustal anomalies could be directly mapped if present. Large crustal remanent fields were found at Mars (Acuña et al., 1998), and it is therefore reasonable to estimate the scale lengths of crustal structures that MESSENGER could resolve. If we assume that only those magnetic features with lateral extent larger than the spacecraft altitude can be resolved, the effective longitudinal and latitudinal resolution is determined strictly by the spacecraft orbit. Fig. 10 illustrates the latitude and longitude resolution afforded by the MESSENGER orbit. The vertical dashed line in Fig. 10 shows the orbit inclination.We expect to be able to resolve magnetic features with horizontal dimensions of 10° (about 400 km) near the periapsis altitude.

7. Summary

A technique has been developed to simulate magnetic field observations at Mercury by the MESSENGER spacecraft, including contributions from an external magnetospheric field to assess the accuracy to which the intrinsic magnetic field structure can be determined with these data. Applied to 12 months of magnetometer data obtained during the orbital phase of the mission, without any correction for the external magnetic field, the planetary moment under the axial-centered-dipole approximation can be determined to better than 5% uncertainty. For an offset dipole the error in the moment is $\sim 10\%$, or about twice as great, and its position is accurate to better than $0.05R_M$. The standard deviations arising from the inversions are much smaller than the results stated above, indicating that the systematic sources of error dominate. Because of the elliptical MESSENGER orbit, the dipole and higher-order terms are highly correlated. This result implies that the surface field variance corresponding to the dipole term error essentially corresponds to the minimum surface field signature that could be attributed to higher-order terms. Improving the dipole accuracy therefore directly corresponds to lowering the detection level for higher-order terms.

The external magnetic field is the primary factor affecting the inversion errors and can be significantly reduced by subtracting an estimate of the external field contribution prior to the inversion. The accuracy in the determinations of the dipole and multipole components of Mercury's magnetic field is therefore tied to the accuracy of the external field model. To maximize the return from the MESSENGER magnetic field investigation, techniques for accurately modeling Mercury's magnetospheric field need to be developed and critically examined. The effects of internal magnetospheric dynamics and differences in the character of the solar-wind magnetosphere interaction at Mercury from that at Earth (the absence of an ionosphere at Mercury and the increased prevalence of subsolar quasi-parallel shock conditions) introduce significant uncertainties in our understanding of Mercury's magnetospheric field. Our ability to characterize reliably the structure of Mercury's intrinsic magnetic field is therefore determined by the extent to which the contributions of these processes to the external field are understood.

Acknowledgements

We thank K.-H. Glassmeier for illuminating discussions on planetary induction currents and O. Aharonson for helpful comments on Runcorn's theorem.We also thank the ACE Team for use of the MAG and SWEPAM data made available via the ACE Level 2 Database. The MESSENGER mission is supported by the NASA Discovery Program under contracts to the Carnegie Institution of Washington (NASW-00002) and The Johns Hopkins University Applied Physics Laboratory (NAS5-97271).

References

Acuña, M.H., Connerney, J.E.P., Wasilewski, P., Lin, R.P., Anderson, K.A., Carlson, C.W., McFadden, J., Curtis, D.W., Mitchell, D., Reme, H., Mazelle, C., Sauvaud, J.A., d'Uston, C., Cros, A., Medale, J.L., Bauer, S.J., Cloutier, P., Mayhew, M., Winterhalter, D., Ness, N.F., 1998. Magnetic field and plasma observations at Mars: initial results of the Mars Global Surveyor mission. Science 279 (5357), 1676–1680.

Aharonson, O., Zuber, M.T., Solomon, S.C., 2004. Crustal remanence in an internally magnetized non-uniform shell: a possible source for Mercury's magnetic field? Earth Planet. Sci. Lett. 218, 261–268.

Bevington, P.R., 1969. Data Reduction and Error Analysis. McGraw-Hill, New York.

Chapman, S., Bartels, J., 1940. Geomagnetism. Oxford University Press, London.

Connerney, J.E.P., 1981. The magnetic field of Jupiter: a generalized inverse approach. J. Geophys. Res. 86 (A9), 7679–7693.

Connerney, J.E.P., Ness, N.F., 1988. Mercury's magnetic field and interior. In: Vilas, F., Chapman, C.R., Matthews, M.S. (Eds.), Mercury. University of Arizona Press, Tucson, pp. 494–513.

Engle, I.M., 1997. Mercury's magnetosphere: another look. Planet. Space Sci. 45 (1), 127–132.

Giampieri, G., Balogh, A., 2001. Modelling of magnetic field measurements at Mercury. Planet. Space Sci. 49, 1637–1642.

Giampieri, G., Balogh, A., 2002. Mercury's thermoelectric dynamo revisited. Planet. Space Sci. 50 (7–8), 757–762.

Glassmeier, K.-H., 2000. Currents in Mercury's Magnetosphere. In: Ohtani, S., Fujii, R., Hesse, M., Lysak, R.L. (Eds.), Magnetospheric Current Systems, Geophysical Monograph, 118. American Geophysical Union, Washington, pp. 371–380.

Gold, R.E., Solomon, S.C., McNutt, R.L., Santo, A.G., Abshire, J.B., Acuña, M.H., Afzal, R.S., Anderson, B.J., Andrews, G.B., Bedini, P.D., Cain, J., Cheng, A.F., Evans, L.G., Feldman, W.C., Follas, R.B., Gloeckler, G., Goldsten, J.O., Hawkins, S.E., Izenberg, N.R., Jaskulek, S.E., Ketchum, E.A., Lankton, M.R., Lohr, D.A., Mauk, B.H., McClintock, W.E., Murchie, S.L., Schlemm, C.E., Smith, D.E., Starr, R.D., Zurbuchen, T.H., 2001. The MESSENGER mission to Mercury: scientific payload. Planet. Space Sci. 49 (14–15), 1467–1479.

Jackson, D.J., Beard, D.B., 1977. The magnetic field of Mercury. J. Geophys. Res. 82 (19), 2828–2836.

Lanczos, C., 1958. Linear systems in self-adjoint form. Am. Math. Monthly 65 (9), 665–679.

Lepping, R.P., Ness, N.F., Behannon, K.W., November 1979. Summary of Mariner 10 magnetic field and trajectory data for Mercury I and III encounters. Technical Memorandum 80600, NASA Goddard Space Flight Center, Greenbelt, MD.

Luhmann, J.G., Russell, C.T., Tsyganenko, N.A., 1998. Disturbances in Mercury's magnetosphere: are the Mariner 10 "substorms" simply driven?. J. Geophys. Res. 103 (A5), 9113–9119.

McComas, D.J., Bame, S.J., Barker, P., Feldman, W.C., Phillips, J.L., Riley, P., Griffee, J.W., 1998. Solar Wind Electron Proton Alpha Monitor (SWEPAM) for the Advanced Composition Explorer. Space Sci. Rev. 86 (1–4), 563–612.

Menke, W., 1984. Geophysical Data Analysis: Discrete Inverse Theory. Academic Press, Orlando, FL.

Ness, N.F., Behannon, K.W., Lepping, R.P., Whang, Y.C., Schatten, K.H., 1974. Magnetic field observations near Mercury: preliminary results from Mariner 10. Science 185 (4146), 151–160.

Ness, N.F., Behannon, K.W., Lepping, R.P., 1975. The magnetic field of Mercury, 1. J. Geophys. Res. 80 (19), 2708–2716.

Ness, N.F., Behannon, K.W., Lepping, R.P., Whang, Y.C., 1976. Observations of Mercury's magnetic field. Icarus 28 (4), 479–488.

Ogilvie, K.W., Scudder, J.D., Hartle, R.E., Siscoe, G.L., Bridge, H.S., Lazarus, A.J., Asbridge, J.R., Bame, S.J., Yeates, C.M., 1975. Observations at Mercury encounter by the plasma science experiment on Mariner 10. Science 185 (4146), 145–151.

Parks, G.K., 1991. Physics of Space Plasmas, An Introduction. Addison-Wesley, New York.

Runcorn, S.K., 1975a. An ancient lunar magnetic dipole field. Nature 253 (5494), 701–703.

Runcorn, S.K., 1975b. On the interpretation of lunar magnetism. Phys. Earth Planet. Inter. 10 (4), 327–335.

Russell, C.T., Baker, D.N., Slavin, J.A., 1988. The magnetosphere of Mercury. In: Vilas, F., Chapman, C.R., Matthews, M.S. (Eds.), Mercury. University of Arizona Press, Tucson, pp. 494–513.

Santo, A.G., Gold, R.E., McNutt, R.L., Solomon, S.C., Ercol, C.J., Farquhar, R.W., Hartka, T.J., Jenkins, J.E., McAdams, J.V., Mosher, L.E., Persons, D.F., Artis, D.A., Bokulic, R.S., Conde, R.F., Dakermanji, G., Goss, M.E., Haley, D.R., Heeres, K.J., Maurer, R.H., Moore, R.C., Rodberg, E.H., Stern, T.G., Wiley, S.R., Williams, B.G., Yen, C.L., Peterson, M.R., 2001. The MESSENGER mission to Mercury: spacecraft and mission design. Planet. Space Sci. 49 (14–15), 1481–1500.

Sibeck, D.G., Lopez, R.E., Roelof, E.C., 1991. Solar wind control of the magnetopause shape, location, and motion. J. Geophys. Res. 96 (A4), 5489–5495.

Siscoe, G.L., Christopher, L., 1975. Variations in the solar wind stand-off distance at Mercury. Geophys. Res. Lett. 2 (4), 158–160.

Slavin, J.A., Holzer, R.E., 1979. The effect of erosion on the solar wind stand-off distance at mercury. J. Geophys. Res. 84 (A5), 2076–2082.

Slavin, J.A., Owen, J.C.J., Connerney, J.E.P., Christon, S.P., 1997. Mariner 10 observations of field-aligned currents at Mercury. Planet. Space Sci. 45 (1), 133–141.

Smith, C.W., Acuña, M.H., Burlaga, L.F., L'Heureux, J., 1998. The ACE magnetic field experiment. Space Sci. Rev. 86 (1–4), 613–632.

Solomon, S.C., 1976. Some aspects of core formation in Mercury. Icarus 28 (4), 509–521.

Solomon, S.C., McNutt, R.L., Gold, R.E., Acuña, M.H., Baker, D.N., Boynton, W.V., Chapman, C.R., Cheng, A.F., Gloeckler, G., Head, J.W., Krimigis, S.M., McClintock, W.E., Murchie, S.L., Peale, S.J., Phillips, R.J., Robinson, M.S., Slavin, J.A., Smith, D.E., Strom, R.G., Trombka, J.I., Zuber, M.T., 2001. The MESSENGER mission to Mercury: scientific objectives and implementation. Planet. Space Sci. 49 (14–15), 1445–1465.

Srnka, L.J., 1976. Magnetic dipole moment of a spherical shell with TRM acquired in a field of internal origin. Phys. Earth Planet. Int. 11 (3), 184–190.

Stephenson, A., 1976. Crustal remanence and the magnetic moment of Mercury. Earth Planet. Sci. Lett. 28 (3), 454–458.

Stevenson, D.J., 1983. Planetary magnetic fields. Rep. Prog. Phys. 46 (5), 555–620.

Stevenson, D.J., 1987. Mercury's magnetic field: a thermoelectric dynamo?. Earth Planet. Sci. Lett. 82 (1–2), 114–120.

Stevenson, D.J., Spohn, T., Schubert, G., 1983. Magnetism and thermal evolution of the terrestrial planets. Icarus 54 (3), 466–489.

Tsyganenko, N.A., 1995. Modeling the Earth's magnetospheric magnetic field confined within a realistic magnetopause. J. Geophys. Res. 100 (A4), 5599–5612.

Tsyganenko, N.A., 1996. Effects of the solar wind conditions on the global magnetospheric configuration as deduced from data-based field models. Technical Report ESA SP-389. European Space Agency, Paris, France, p. 181.

Whang, Y.C., 1977. Magnetospheric magnetic field of Mercury. J. Geophys. Res. 82 (7), 1024–1030.